AA22 - Bayer Process Heat Exchanger Tube with High Corrosion Resistance in Diluted Sulphuric Acid

Darwin Del Aguila[1] and Joseph Del Aguila[2]
1. Aushex Pty Ltd, Corrosion Scientist, Brisbane, Australia
2. Aushex Pty Ltd, Director, Brisbane, Australia
Corresponding author: d.delaguila@aushex.com

Abstract

The objective of this research was to increase the corrosion resistance of the low carbon steel heat exchanger tube used in the Bayer Process. In this application, the tubes are exposed to 6 % sulphuric acid during the regular acid wash of heat exchanger trains to remove DSP formation. By achieving this objective, the lifespan of the tube is increased by up to a factor of 3-4. This improvement reduces maintenance costs and increases alumina production. At the beginning of 2015, a tube sample (referred to as "Special 42") was accidentally found at the mill facility with a low-quality type microstructure characterized as "partially dispersed cementite" instead of "spheroidised and fully dispersed cementite" which is the specification for this industry. However, when tested, this "Special 42" sample exhibited outstanding corrosion resistance to dilute sulphuric acid. Since then, this sample has constituted the source for further research work. Now, we can confidently say that while spheroidised microstructure does contribute to the increased corrosion resistance of low carbon steel, its impact is much less compared to another metallurgical parameter discovered in 2016 and successfully implemented from the laboratory to the tube production line in the middle of 2017. This new metallurgical parameter is related to a particular grain orientation of the substrate that enhances the formation of a high transfer resistance passive film and consequently inhibits corrosion attack. This new material, now named "Superhex", has been prepared with different microstructures likely to be found in a typical ASTM 179/192 and evaluated together with current materials under harsh corrosion conditions. The laboratory results indicate a 4-15% mass loss for the Superhex, compared to 26-55 % and 58-95 % mass loss for the Current Alumina Refineries and STD ASTM 179 tube materials, respectively.

Keywords: Sulphuric acid, corrosion resistance, ASTM 179, heat exchanger tube.

1. Introduction

In its dilute form, sulphuric acid reacts with metals (e.g. iron) through Equation (1) producing hydrogen (gas) and metal sulphate (salt) on the metal surface [1,2,3] given by Equation (1):

$$Fe_{(s)} + H_2SO_{4\,(aq)} \rightarrow H_{2\,(g)} + FeSO_{4\,(aq)} \qquad (1)$$

Recent advanced technology on crystallography and passivation film has identified key metallurgical parameters that can provide high corrosion resistance in acid solutions. Figure 1 shows an example of the in-laboratory behaviours of two cold-drawn low-carbon steel ASTM-179 tubes, with preferred versus unpreferred crystal grain orientation condition, after 15 h exposure to 6 % v/v uninhibited sulphuric acid at 60 °C and flow rate of 1 m/s. Significant corrosion of the unpreferred orientation (STD ASTM 179) with 94.3 % mass loss in comparison to the relatively unaffected preferred orientation (Superhex) with only 5.5 % mass loss.

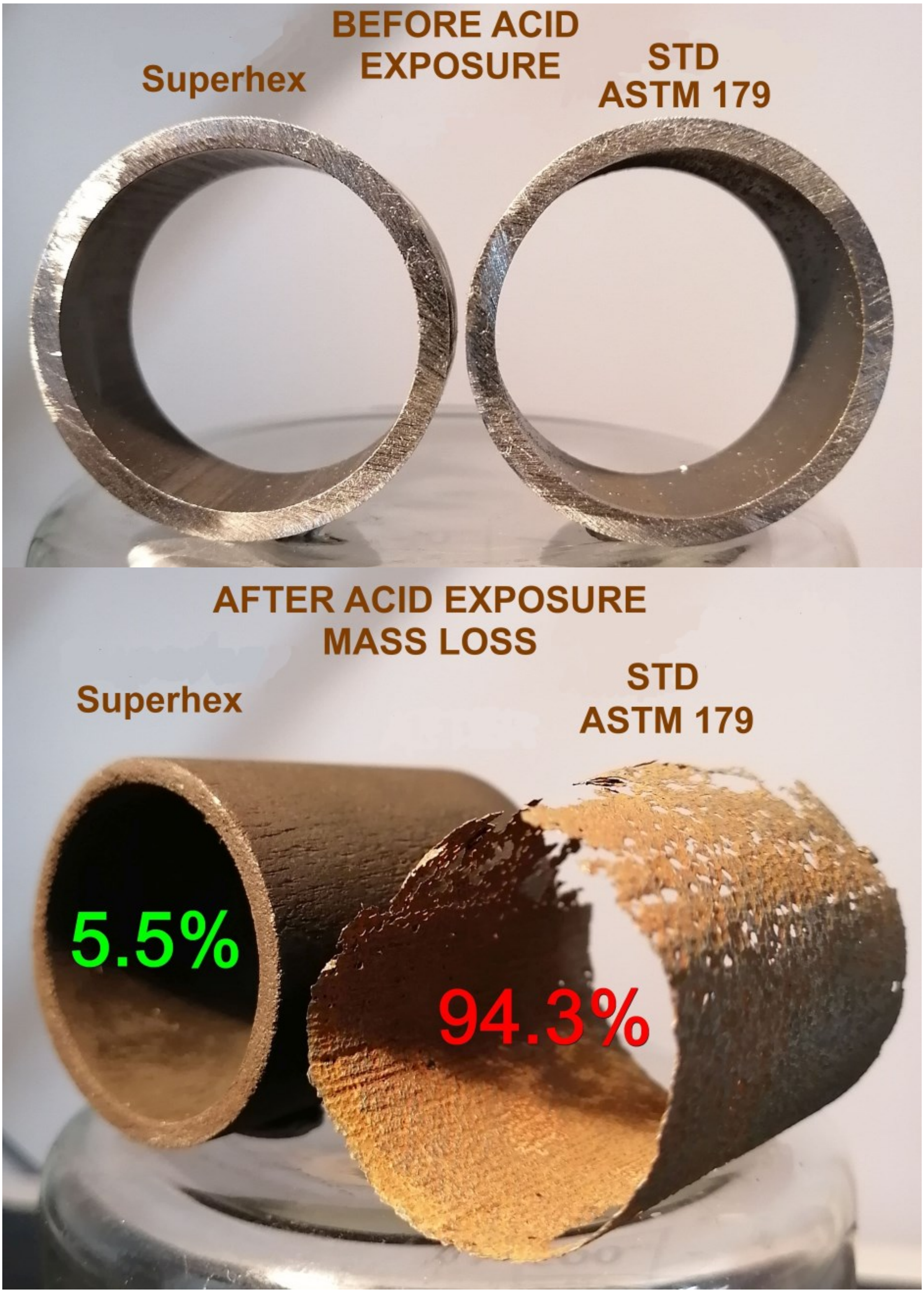

Figure 1. Mass loss images of Superhex vs STD ASTM 179.

To investigate the above phenomena electrochemical measurement techniques, such as impedance spectroscopy and polarization resistance, are accordingly considered as useful corrosion monitoring practices to track changes in mechanisms. Also, they could be successfully employed for detecting large changes in corrosion rates where obtaining very accurate values is not necessary, i.e. for comparison purposes [4-6].

2. Experimental

The sample STD ASTM 179 has been supplied by an Australian alumina refinery and the Superhex sample is the Aushex' product in its final manufacturing process currently been supplied to one alumina refinery in Australia and Brasil respectively. The tube manufacturing processes of the studied hex tubes were as below:

I) Piercing of the billet at 1,200 °C for a short time, II) first cold drawing, III) second cold drawing (final size 38.1 × 2.6 mm), IV) spheroidization treatment at 780 °C for 4 h; ferritic-pearlitic tubes were normalized at the same temperature for 20 min. The chemical compositions and microstructural characteristics of the materials are provided in Table 1.

Table 1. Chemical composition and microstructure of materials.

Materials	Microstructure	Chemical Composition (wt %)				
		C	Si	Mn	P	S
Superhex	Partially Spheroidised	0.102	0.243	0.491	0.008	0.004
STD ASTM 179	Pearlitic	0.117	0.226	0.353	0.012	0.001

Several cut-offs from as-received tubes of the studied materials were prepared for microstructural and electrochemical studies as described below.

2.1 Sample Preparation

Two pairs of cut-off coupons of STD ASTM 179 and Superhex samples were selected and mounted into I) a conductive resin, and II) a non-conductive resin to provide suitable specimens for microstructural and corrosion studies. Both pairs were mechanically wet ground and polished down to 0.04 µm using standard procedures in colloidal silica, washed with ethanol, and dried in the air. The coupons mounted in conductive resin were used for pre-exposure microanalysis and therefore were not subjected to corrosion. The other pair was used to monitor the impact of the corrosive medium on the as-polished surfaces by submerging them in 6% v/v uninhibited sulphuric acid at 60 °C for 10 min for static corrosion investigation. This pair was then re-polished and submerged in the acid solution for electrochemical analysis.

2.2 Microstructural Investigation

2.2.1 Scanning Electron Microscopy and EBSD

The pre-exposure microstructure was studied using a Field Emission Scanning Electron Microscope (FE-SEM) machine model JEOL 7001F, with automated feature detection equipped with secondary electron and Energy Dispersive X-ray Spectroscopy (EDS) analysis system, OXFORD Electron Back-Scatter Diffraction (EBSD) pattern analyzer and Channel 5 analysis software. Strain contouring component of OXFORD Channel 5 software was employed to estimate the extent of deformation, or strain, in individual grains in EBSD maps. Maps were obtained using an accelerating voltage of 25 kV and a step size of 0.9 µm at 700× magnification. To reveal carbides in the ferritic-pearlitic and spheroidized microstructures resulted from the discussed heat treatment processes, samples mounted in the conductive resin were also etched in

10 ml glycerin + 6 ml HCl + 3 ml HNO3 solution for 10 s. This was done as complementary to EBSD since it is not capable of revealing pearlitic structures in steels. SEM images were also obtained immediately (in the first few hours) after the exposure of electrochemical samples in secondary electron mode.

2.2.2. Optical Microscopy Analysis

Corrosion attack sites and microstructures were immediately observed on as-polished samples after 10 min exposure to the sulphuric acid solution using an optical microscope model Leica DMi8A with the magnification range of 2.5× to 50× equipped with Leica Application Suite software.

2.3 Electrochemical Investigation

Electrochemical experiments were conducted (on as-polished samples) using a three-electrode cell containing 6 % v/v uninhibited sulphuric acid at 60 °C using a VMP3-based BioLogic instrument controlled by EC-Lab® software. Test coupons were subjected to Open Circuit Potential (OCP), Electrochemical Impedance Spectroscopy (EIS), Linear Polarization Resistance (LPR), and Potentiodynamic Polarization (PDP) measurements. Before experiments, specimens were mounted in a non-conductive resin (exposing 0.27 and 0.29 cm^2 of the surfaces of STD and Superhex samples, respectively) and then polished as discussed in section 2.1. A platinum sheet was used as a counter electrode, a standard Ag/AgCl (VL_Ionode004) as a reference electrode with the sample of interest as a working electrode. Electrochemical measurements were carried out in the following order for each sample:

OCP was measured for 90 min after the immersion of samples into the acid solution. EIS measurements were then obtained using a frequency range of 100 kHz to 100 Mhz with the amplitude of ±10 mV. EIS measurements were repeated 3 times at 5-min intervals for each sample. LPR measurements were run afterward at the potential scan rate of 0.1 mV/s and the potential range of - 25 to + 25 mV concerning OCP. Finally, PDP was conducted at the potential scan rate of 10 mV/min and a potential range of -200 to +500 mV concerning the open circuit potential. ZFit analysis of EC-Lab® software was used to fit successive impedance cycles. LPR plots were analyzed using the polarization resistance (RP) fit tool of EC-Lab® software to calculate Rp, corrosion current density (icorr), and corrosion potential (Ecorr) values within ± 20 mV from the corrosion potential. PDP plots were also analyzed using the software's Tafel fit tool to calculate Tafel slopes (βa and βc), icorr, and Ecorr values.

3. Results

3.1 Pre-exposure Microstructure

Optical and SEM images of etched samples (Figure 2), as well as EBSD maps of polished and mirror-like samples (Figure 3), show a texture consisting of pearlites (α + Fe_3C) distributed through coarse grains of ferritic iron (α) with particles of cementite (Fe_3C) mostly dispersed along grain boundaries (GB) for Superhex sample. Remaining pearlites here point to the fact that the spheroidization process was not 100 % complete. On the other hand, relatively fine-grained pro eutectoid ferrite (α) with a higher fraction of pearlites (α + Fe_3C) is observed for the STD ASTM 179 sample. Table 2 shows the fraction of phases extracted from EBSD mappings. GB carbide (cementite) in the pearlitic sample is around twice of that in the spheroidized sample. The fraction of zero solution areas (white areas in-band contrast and black areas in phase map images of Figure 3) in both samples could point to the lamellar pearlitic structure which is hard to detect with EBSD.

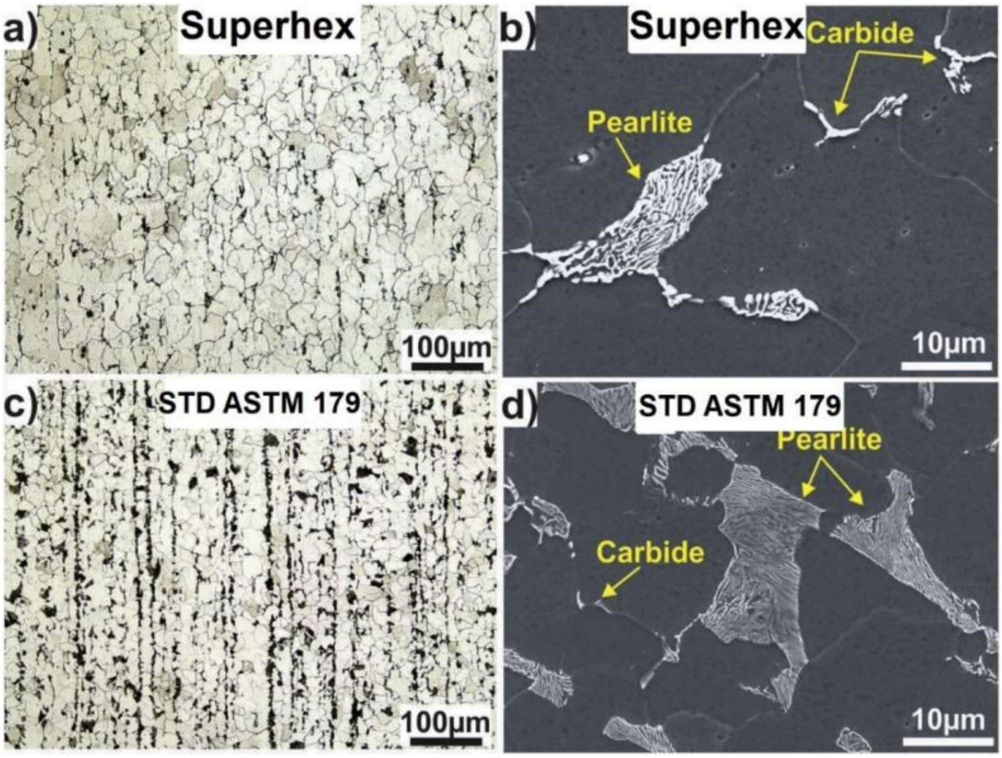

Figure 2. Optical (left) and SEM (right) images of as received.

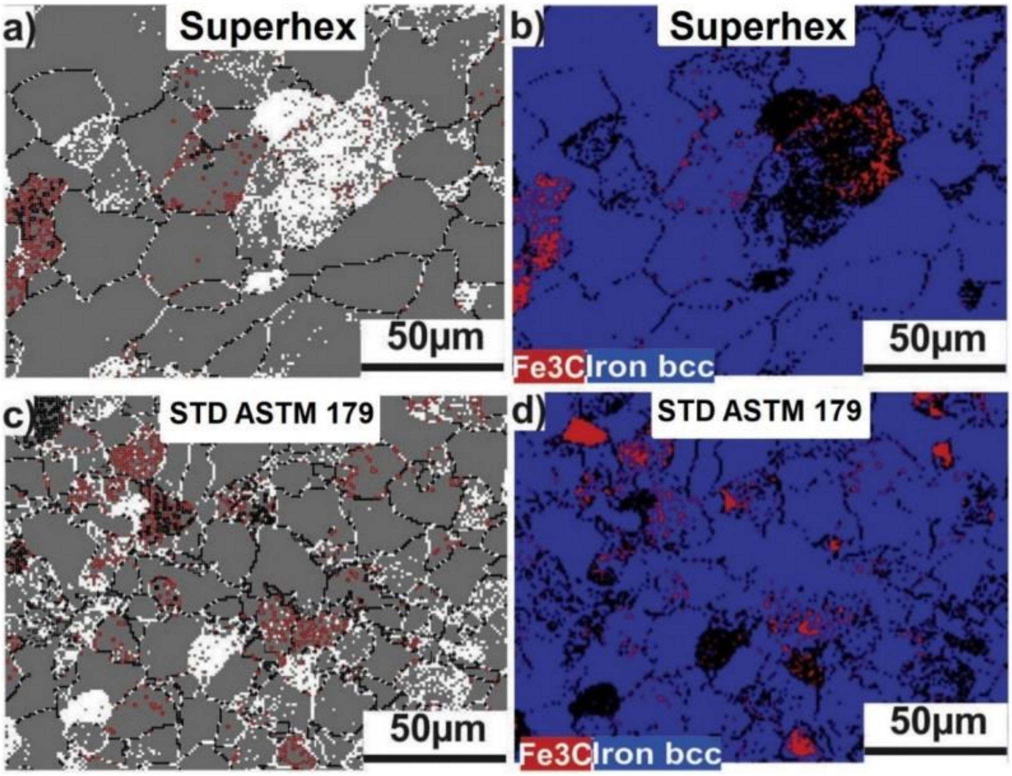

Figure 3. EBSD band contrast (left), EBSD phase map (right).

EBSD strain contouring maps in Figure 4 show that the maximum of lattice strain for STD ASTM 179 sample ($\simeq 2$) is almost 10 times that for the Superhex sample ($\simeq 0.2$). This means that STD ASTM 179 has led to significant stress relieving resulted in lower amounts of residual stresses remaining in the matrix compared to the pearlitic sample.

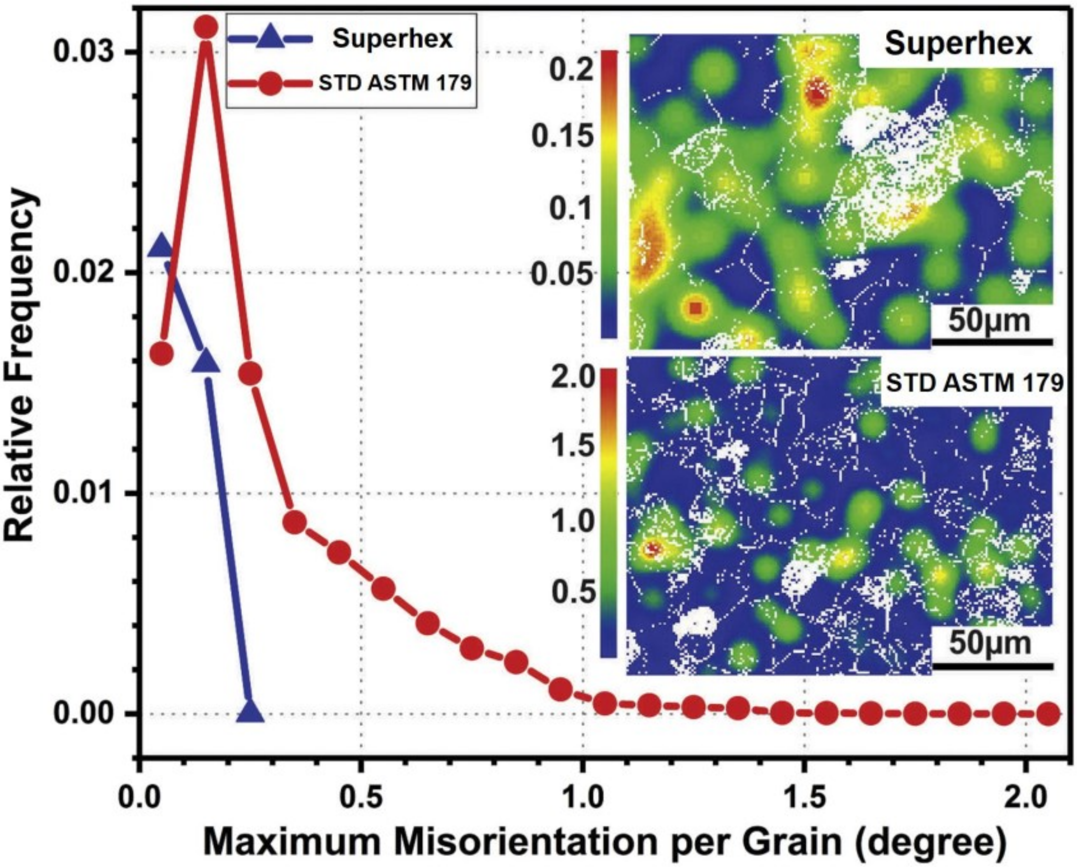

Figure 4. EBSD strain contouring maps showing lattice strain.

Table 2. Phase fraction resulted from EBSD.

Phase	**Phase Fraction (%)**	
	Superhex	STD ASTM 179
Fe_3C	2.76	4.62
Ferrite (iron bcc)	83.64	80.02
Zero solution	13.6	15.37

3.2 Static Corrosion Behaviour

To investigate the impact of the corrosive solution on the material surface, as-polished mirror-like surface samples were subjected to 6 % v/v uninhibited sulphuric acid for 10 min and then examined immediately under a light microscope. Low and high magnification optical microscopy images of the Superhex sample are shown in Figure 5 (a to c). The image shows that the acid attacks selective areas on the surface. These areas are mostly corresponding to GBs and the interfaces between cementite and ferrite (see Figure 2 and Figure 3). Images of the STD ASTM 179 sample in Figure 5 (d to f) show more serious corrosion (compared to the Superhex sample on the left) with a similar GB attack.

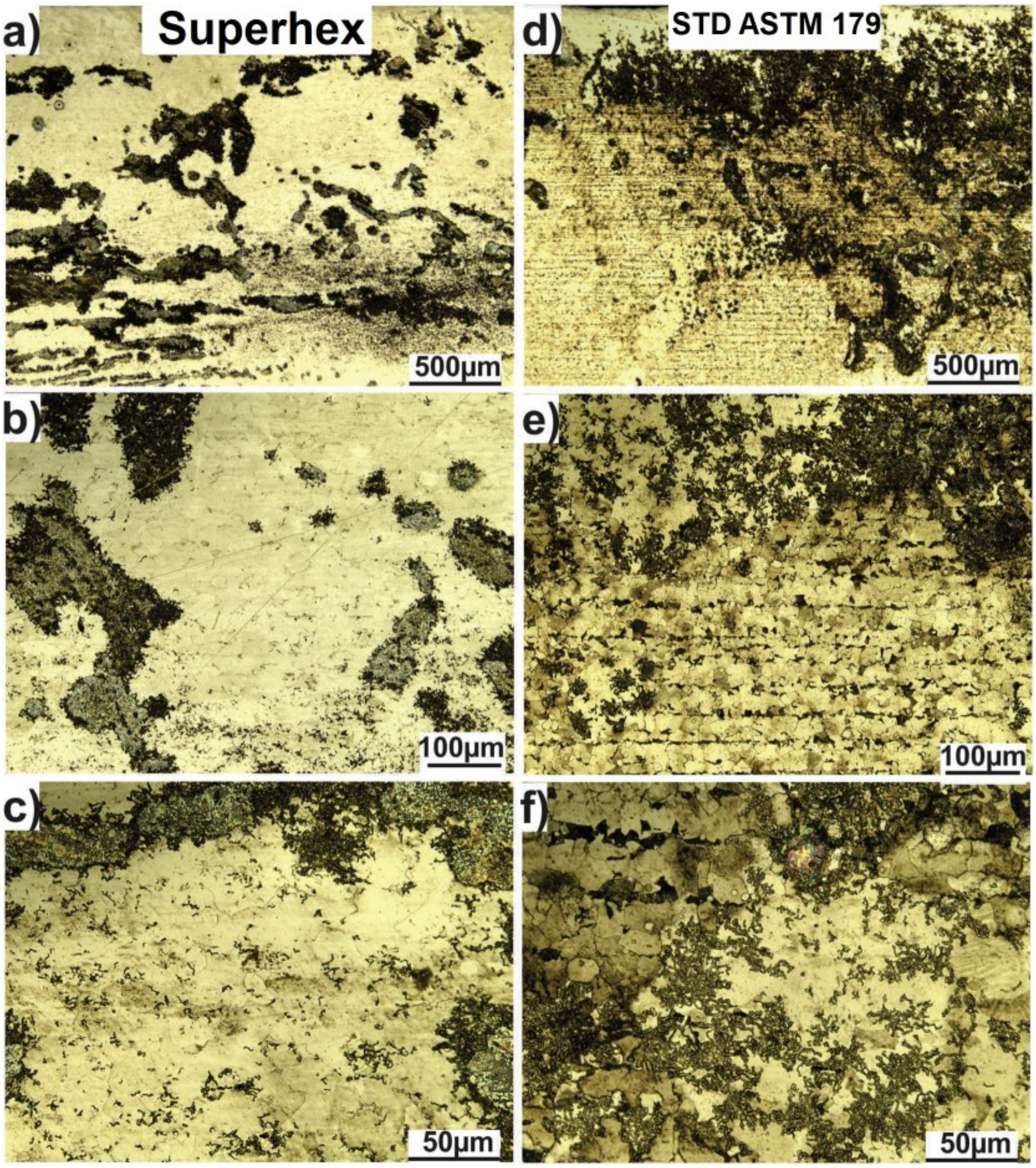

Figure 5. Low and high magnification optical images of Superhex sample (a) to (c), and STD ASTM 179 sample (d) to (f).

3.3 Electrochemical Behaviour

Open Circuit Potentials (OCP) of the samples in 6 % v/v uninhibited sulphuric acid at 60 °C are shown in Figure 6a. Both samples show an active behavior in the first 500 s of exposure. The Superhex sample then tends to stabilize at around -490 mV while the STD ASTM 179 sample gains nobler potential values over time but is not stabilized even after 90 min (5400 s) of exposure.

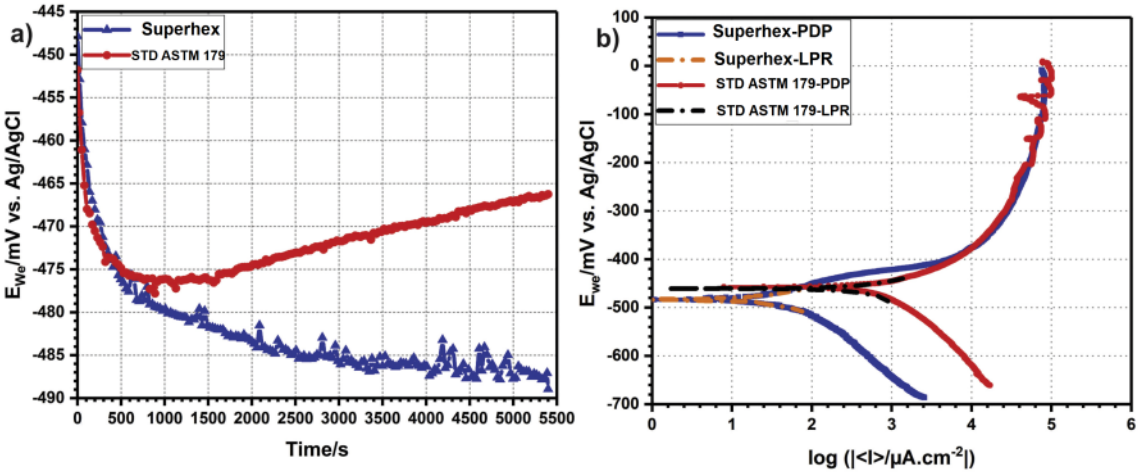

Figure 6. (a) OCP, and (b) PDP. Dash-dot lines in (b) show Evans diagrams (E-logi).

Ecorr values in E-logi plots (PDP and LPR) shown in Fig. 6b reflects OCP values in Figure 6a. Figure 7 also shows LPR plots (E vs. i) of the test samples in the corrosive medium. Data extracted from PDP and LPR curves are summarized in Table 4.

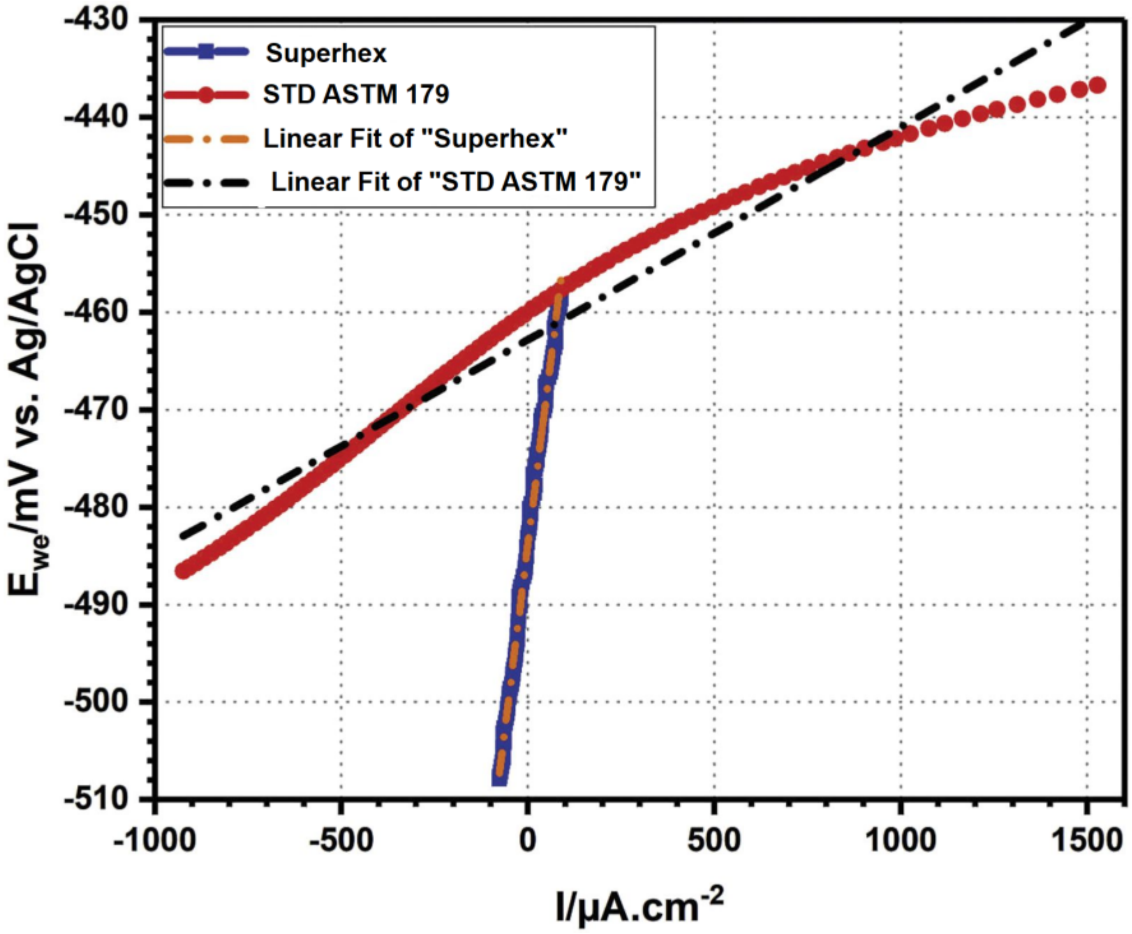

Figure 7. Linear polarization resistance (LPR) curves of the samples in 6% v/v in uninhibited sulphuric acid.

Polarization resistance (Rp) is defined as the slope of potential vs. current density curve, Figure 7, at the free corrosion potential according to Faraday's law [3,5] given in Equation (2):

$$Rp = \left(\frac{dE}{di}\right) Ecorr \tag{2}$$

Where:
E Corrosion potential
i Corrosion current.

Corrosion current density (icorr) is then calculated according to the Stern-Geary relationship [6, 7] given in Equation (3):

$$icorr = \frac{\beta a . \beta c}{Rp(\beta a + \beta c) \ln 10} \tag{3}$$

Where:
βa and *βc* Tafel slopes anodic and cathodic. Calculated with the fitting of PDP curves given in Table 4.

Figure 7 and data in Table 4 show a much higher Rp value for the Superhex sample with an RP drop of around 93% for the STD ASTM 179 sample. This is in agreement with the noticeable rise in icorr values (separate calculations from PDP and LPR measurements, see Table 4) and the accompanied steeper Tafel slopes in both cathodic and anodic branches of the STD ASTM 179 sample compared to the Superhex one. This suggests that different mechanisms control corrosion of the samples here.
Corrosion current density corresponds to corrosion rate (CR) according to [5, 8] given in Equation (4):

$$CR = K.EW.\frac{icorr}{\rho} \tag{4}$$

Where:
K = 3.272e-3 mm.g.µA-1.cm-1.yr-1
EW = Equivalent weight (= 27.92 for carbon steel [24])
ρ = Density of iron = 7.87 g.cm^{-3}.

CR values extracted directly from PDP measurements as well as those from LPR are also shown in Table 4. Accordingly, the STD ASTM 179 sample is shown to corrode around 21 times faster than the Superhex one. It is worth noting that the CR values reported here only indicate the initial corrosion rates and no long-term corrosion measurement was conducted in this study.

To further understand the mechanisms of corrosion, EIS was measured immediately after OCP and repeated 3 times at 5-min intervals. Nyquist and Bode-Phase plots in Figure 8 and Figure 9 confirm much higher polarization resistance (Rp) of the Superhex sample 6 % v/v sulfuric acid compared to that of the STD one. Also, the repetition of EIS confirms that the Superhex sample has been well stabilized after 90 min exposure, whereas the STD sample is still active with a continuous reduction of Rp over time (diameters of the capacitive loops in Figure 8b).

Nyquist plots in Figure 8 were successfully fit (only the last curve, 10 min, for each sample) using the indicated equivalent circuits with the extracted data summarized in Table 3. Here Rs, Rct, and RL point to solution resistance, charge transfer resistance, and inductance resistance, respectively. Qdl is the double layer Constant Phase Element (CPE), which points to the non-ideal capacitance of the surface and is used to calculate the surface charge transfer capacitance during corrosion [31], while n represents the CPE parameter.

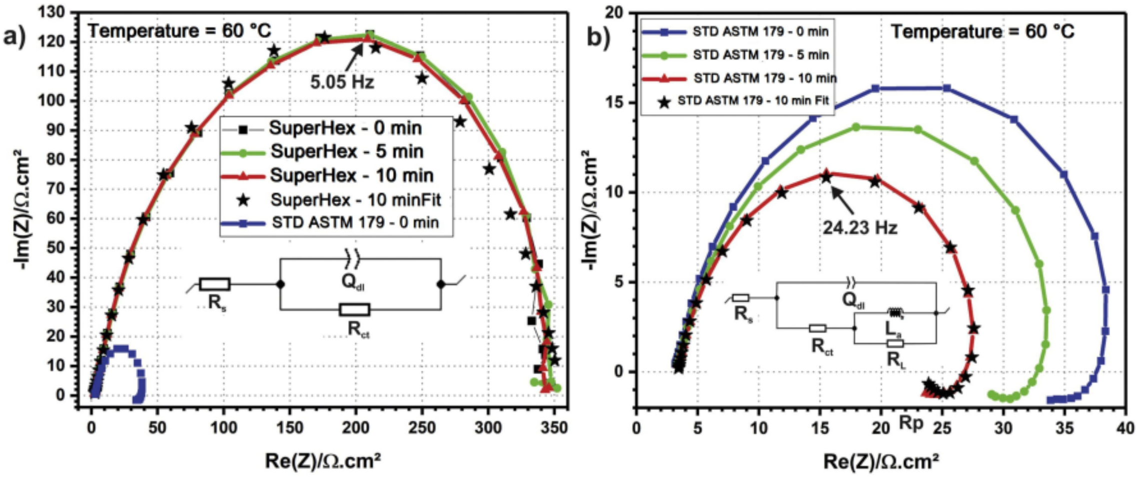

Figure 8. Nyquist plots (a) Superhex and (b) STD ASTM 179 samples along with calculated equivalent circuits and fit data points for the third (10 min) plots.

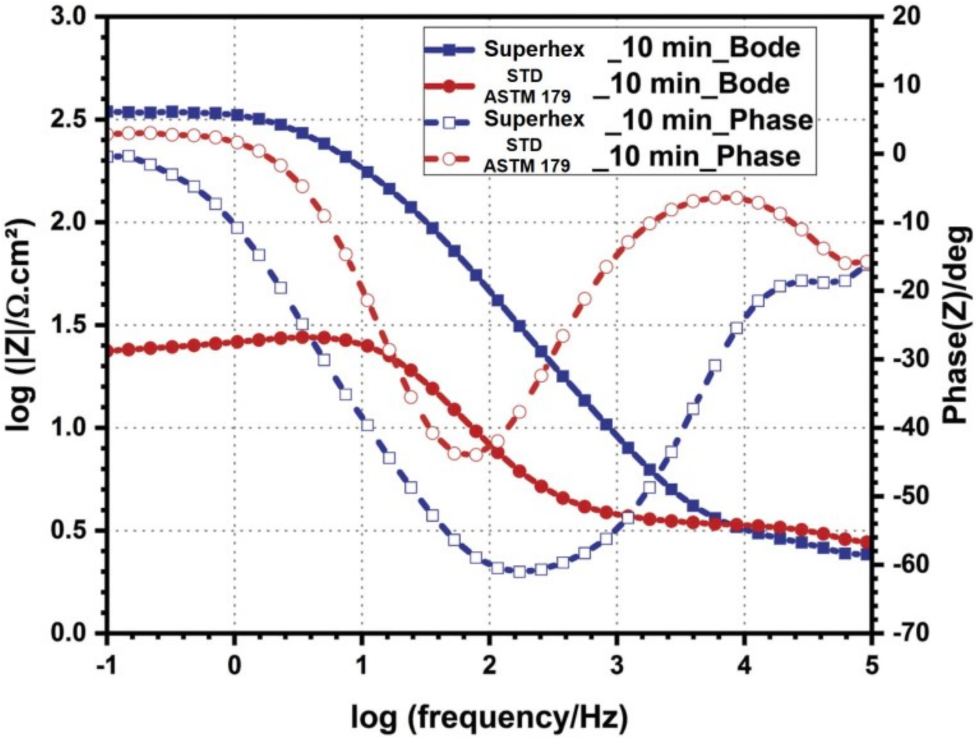

Figure 9. Bode-phase plots of the samples corresponding to the third (10 min) Nyquist plots in Figure 8.

The difference in mechanisms is illustrated in the EIS clearly by the Superhex sample detected fitting a Randles-like equivalent circuit with a semicircle and one time constant while an inductive loop appears for the STD sample with a modified inductance (La) at low frequencies. It is noteworthy that modified inductance could be used as an element with positive values in an equivalent circuit to avoid interpreting negative values associated with some inductive loops [9]. The impedance of an inductance (ZL) is expressed as [10-11] given by Equation (5):

$$ZL(j\omega) = Lj\omega \tag{5}$$

Where:
L Inductance
$J = \sqrt{-1}$
$\omega = 2\pi f$
$F =$ Frequency in Hz

The impedance of a modified inductance (La) is then expressed as [11] given by the Equation (6):

$$ZLa(j\omega) = La(j\omega)^{aL} \tag{6}$$

Where:
aL Represents the *La* parameter (if aL=1 then La≡L).

Table 3. Data extracted from equivalent circuit models used to fit the curves in Figure 8.

	R_{s} [Ω.cm^2]	R_{ct} [Ω.cm2]	Q_{dl} [F.s^{n-1}.cm^{-2}]	n_{dl}	L_{a} [H.s^{a-1}.cm^2]	a_{L}	R_{L} [Ω.cm^2]
Superhex	2.4	353.2	1.50E-04	0.77	---	---	---
STD ASTM 179	3.4	19.9	5.90E-04	0.86	1.4	0.7	8.4

Polarization resistance Rp could be also calculated from data in Table 3

Where:
Rp = Rct For the Superhex sample
Rp = Rct + RL. For the STD sample,

These values (which are also shown in Table 4) are correspondingly in good agreement with those of the LPR measurement in Table 4.

Table 4. Data extracted from PDP, LPR, and EIS curves in Figure 6b, Figure 7, and Figure 8, respectively.

	E_{corr}		βa	βc	i_{corr}		Rp		*CR*	
	[mV vs. Ag/AgCl]		mV/dec		[μA.cm^{-2}]		[Ω.cm^2]		mm/year	
Source	PDP	LPR	PDP	PDP	PDP	LPR	LPR	EIS	PDP	LPR
Superhex	-483	-484	69.4	140.6	66.6	64.5	313.0	353.2	0.78	0.76
STD ASTM 179	-458	-462	130.5	180	1386.2	1415.1	23.2	28.3	16.24	16.57

4. Discussion

As shown in Figure 2 and Figure 3, the STD ASTM 179 sample contains finer grains resembling an increased GB length (per unit volume) compared to the Superhex sample. The higher fraction of pearlites (and subsequently the interface of cementite/ferrite) and GB carbides along with increased GB length lead to a heterogeneous microstructure in the STD ASTM 179 sample. Therefore, the microstructure of this metal is expected to be more susceptible to localized attack, mainly because of the formation of micro-anodes/cathodes on the surface [12, 13], compared to the Superhex structure with coarse pro eutectoid ferrites.

The higher amount of lattice strain and subsequently residual stresses in the STD sample implies less thermodynamic stability compared to the Superhex sample. This could be confirmed through OCP plots and 5-min interval impedance measurements as shown in Figure 6a and Figure 8. Such instability could also provide the driving force for corrosion and contribute to the higher corrosion rate and/or lower polarization resistance (see Table 4) of the STD sample as confirmed by PDP and LPR measurements in Fig. 6b and Figure 7, respectively.

Noticeable discrepancies between the Tafel slopes (βa and βc) and Rp values of the samples indicate a significant difference in corrosion kinetics. According to Equation (1), and insoluble iron sulfate ($FeSO_4$) is likely to precipitate on the surface of the metal [1, 2, 3]. This involves the simultaneous exchange of electrons through the oxidation of metal (anodic reaction) and reduction of hydrogen (cathodic reaction) according to the below reactions, respectively [3] given by Equations (7) and (8):

$$Fe \rightarrow Fe^{2+} + 2e^{-} \tag{7}$$

$$2H^{+} + 2e^{-} \rightarrow H_2 \tag{8}$$

Accordingly, Superhex metallurgy seems to lead to significant reductions in both metal dissolution and hydrogen evolution rates of the steel, see Tafel slopes in Table 4. Such a transition is actually because of a change in the mechanism of corrosion as shown by Nyquist plots and their corresponding equivalent circuits in Figure 8. Impedance spectra show that the corrosion of the Superhex sample is under charge transfer (activation) control with a large capacitive loop (high Rp value). However, the diameter of the semicircle significantly reduces for the STD sample (low Rp value) while an inductive loop appears in its low-frequency region which indicates adsorption (precipitation) following the Volmer-Heyrovský mechanism [14-15].

Heterogeneity of microstructure, due to the presence of either polycrystalline metal surfaces (various crystals and grains) or crystal defects (such as GBs, dislocations, point defects, etc.), can increase the level of surface energy stored in the material [16-17]. Here, the STD sample contains both the polycrystalline surface (increased number of grains with high fractions of pearlites and carbides) and crystal defects (due to the presence of residual stresses resulted from lattice strain together with the increased GB length). These are the areas that are susceptible to be preferentially attacked by the corrosive solution. Optical microscopy images in Figure 5 confirm the above.

5. Conclusions

A combination of microstructural and electrochemical investigations was carried out to analyze the impact of 6 % v/v uninhibited sulphuric acid on carbon steel A179 with a pearlitic-ferritic structure compared to when heat treated to a spheroidized structure.

Electron Back-Scatter Diffraction, Optical and Scanning Electron Microscopy observations showed a more heterogeneous microstructure containing fine ferrite and pearlite grains with an increased grain boundary length and lattice defects (lattice strain) for the STD metal compared to the Superhex condition.

Electrochemical Impedance Spectroscopy and Linear Polarization Resistance measurements showed different mechanisms for the corrosion of the samples with a much lower polarization resistance in the absence of stabilization for the Superhex sample. Accordingly, polarization showed that Superhex metallurgy has led to a 21 times reduction in the corrosion rate. This was further shown to result from a reduction in the kinetics of both anodic and cathodic reactions.

Further microscopical observations showed higher amounts of precipitates and higher amounts of corrosion on the surface of the STD sample. Finally, Superhex metallurgy was found to lead to a more homogeneous microstructure that de-risks the formation of micro-anodic/cathodic sites on the surface of the metal and significantly improves the corrosion performance.

6. Acknowledgment

The data reported in the paper were obtained at the Central Analytical Research Facility (CARF) operated by the Institute for Future Environments (IFE) at Queensland University of Technology (QUT). Access to CARF was supported by funding from the Science and Engineering Faculty, QUT. The commercial tube materials were supplied by the Australian alumina refinery. This research did not receive any specific grant from funding agencies in the public, commercial, or not-for-profit sectors.

7. References

1. M.G. Fontana, *Corrosion Engineering*, 3 edddition, McGraw-Hill Book Company1985.
2. M.J. King, W.G. Davenport, M.S. Moats, *Materials of Construction, Sulfuric Acid Manufacture - Analysis, Control, and Optimization* (2nd Edition), *Elsevier*, San Diego, Calif, 2013, pp. 349-356.
3. S. Lyon, Overview of corrosion engineering, science and technology, Nuclear Corrosion Science and Engineering, *Elsevier* Ltd., 2012, pp. 3-30.
4. F. Mansfeld, Tafel slopes and corrosion rates obtained in the pre-Tafel region of polarization curves, *Corrosion Science*, 47 (2005) 3178-3186.
5. ASTM G102-89, Standard practice for calculation of corrosion rates and related information from electrochemical measurements, *ASTM International*, West Conshohocken, PA, 2015.
6. ASTM G59-97, Standard Test Method for Conducting Potentiodynamic Polarization Resistance Measurements, *ASTM International*, West Conshohocken, PA, 2014.
7. ASTM G3-14, Standard Practice for Conventions Applicable to Electrochemical Measurements in Corrosion Testing, *ASTM International*, West Conshohocken, PA, 2014.
8. K. Vignarooban, P. Pugazhendhi, C. Tucker, D. Gervasio, A.M. Kannan, Corrosion resistance of Hastelloys in molten metal-chloride heat-transfer fluids for concentrating solar power applications, *Solar Energy*, 103, 2014, 62-69.
9. The modified inductance element La, Application Note 42, *Bio-Logic Science Instruments*, 2012.
10. S. Ramanathan, Negative Resistances and Inductances in Equivalent Circuits for Adsorption-Reaction Kinetics, *ECS Transactions*, 33, 2011, 21-35.
11. C. Gabrielli, M. Keddam, H. Takenouti, The Use of a.c. Techniques in the Study of Corrosion and Passivity, 23, 1983, 395-451.
12. D. Clover, B. Kinsella, B. Pejcic, R. De Marco, The influence of microstructure on the corrosion rate of various carbon steels, *J. Appl Electrochemistry*, 35, 2005, 139-149.
13. Q.Y. Pan, W.D. Huang, R.G. Song, Y.H. Zhou, G.L. Zhang, The improvement of localized corrosion resistance in sensitized stainless steel by laser surface remelting, *Surface and Coatings Technology*, 102, 1998, 245-255.
14. J.P. Diard, P. Landaud, B. Le Gorrec, C. Montella, Calculation, simulation and interpretation of electrochemical impedance. Part II. Interpretation of Volmer-Heyrovsky impedance diagrams, *Journal of Electroanalytical Chemistry and Interfacial Electrochemistry*, 255, 1988, 1-20.
15. F. Mansfeld, Analysis and Interpretation of EIS Data for Metals and Alloys, Technical Report No. 26, University of Southern California, Los Angeles, CA, USA, 1999.
16. H.P. Stüwe, A.F. Padilha, F. Siciliano, Competition between recovery and recrystallization, *Materials Science and Engineering,* A, 333, 2002, 361-367.
17. D. Raabe, Recovery and Recrystallization: Phenomena, Physics, Models, Simulation, in D.E.L. Hono (Ed.), *Physical Metallurgy* (Fifth Edition), Elsevier, Oxford, 2014, pp. 2291-2397.